New Insight into the Local Structure of Hydrous Ferric Arsenate Using Full-Potential Multiple Scattering Analysis, Density Functional Theory Calculations, and Vibrational Spectroscopy

Shaofeng Wang, Xu Ma, Guoqing Zhang, Yongfeng Jia, Keisuke Hatada

1   **New insight into the local structure of hydrous ferric arsenate using**

2   **full-potential multiple scattering analysis, density functional theory calculations,**

3   **and vibrational spectroscopy**

4

5   Shaofeng Wang[1], Xu Ma[1], Guoqing Zhang[1], Yongfeng Jia[2, *], Keisuke Hatada[3]

6

7   1. Key Laboratory of Pollution Ecology and Environmental Engineering, Institute of

8   Applied Ecology, Chinese Academy of Sciences, Shenyang, 110016, China

9   2. Institute of Environmental Protection, Shenyang University of Chemical

10   Technology, Shenyang, 110142, China

11   3. Département Matériaux Nanosciences, Institut de Physique de Rennes, UMR

12   UR1-CNRS 6251, Université de Rennes 1, 35042 Rennes Cedex, France

13   * Corresponding author, Prof. Yonfeng Jia, Email: yongfeng.jia@iae.ac.cn, Tel: +86

14   (24) 83970503

15

16   TOC art

17

18
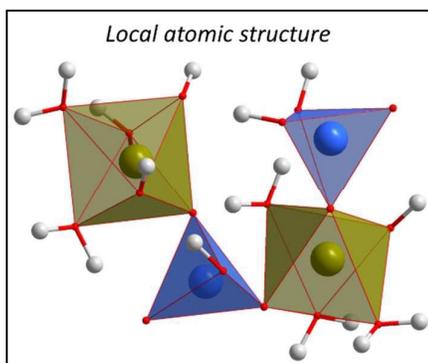
Local atomic structure

19   **ABSTRACT:** Hydrous ferric arsenate (HFA) is an important arsenic-bearing

20   precipitate in the mining-impacted environment and hydrometallurgical tailings.

21   However, there is no agreement on its local atomic structure. The local structure of

22   HFA was re-probed by employing a full-potential multiple scattering (FPMS)

23   analysis, density functional theory (DFT) calculations, and vibrational spectroscopy.

24   The FPMS simulations indicated that the coordination number of the As-Fe and/or

25   Fe-As in HFA was approximately two. The DFT calculations constructed a structure

26   of HFA with the formula of $Fe(HAsO_4)_x(H_2AsO_4)_{1-x}(OH)_y \cdot zH_2O$. The presence of

27   protonated arsenate in HFA was also evidenced by vibrational spectroscopy. The As

28   and Fe K-edge XANES spectra of HFA were accurately reproduced by FPMS

29   simulations using the chain structure, which was also a reasonable model for EXAFS

30   fitting. The FPMS refinements indicated that the interatomic Fe-Fe distance was

31   approximately 5.2 Å, consistent with that obtained by Mikutta et al. (*ES&T*, 2013)

32   using wavelet analysis. All of the results suggested that HFA was more likely to

33   occur as a chain with AsO_4 tetrahedra and FeO_6 octahedra connecting alternately in

34   an isolated bidentate-type fashion. This finding is of significance for understanding

35   the fate of arsenic and the formation of ferric arsenate minerals in an acidic

36   environment.

37

INTRODUCTION

Hydrous ferric arsenate (HFA) is one of the important secondary arsenic precipitates in the mining-impacted environment and hydrometallurgical tailings,[1-5] such as acidic mining drainage [6] and gold[7] and uranium mine tailings.[4, 8, 9] In the Fe-As coprecipitation process, a widely employed method for the removal and fixation of arsenic from hydrometallurgical raffinates, HFA precipitates as a major arsenic-bearing phase at acidic pH values.[10] The adsorbed arsenate on ferrihydrite was also observed to transform into HFA at pH values of 3-5.[2, 3] HFA is thermodynamically metastable and can convert to scorodite during prolonged aging at ambient temperature[5] or elevated temperatures.[3, 11] Therefore, precipitation of HFA followed by heat treatment was also employed for the synthesis of scorodite,[1, 4, 12-14] and this could provide an alternative method for the removal and fixation of arsenic in hydrometallurgical solutions with conventional autoclave[15] and ambient pressure scorodite precipitation technology.[16-18]

The local atomic structure of HFA controls its environmental behaviors and recrystallization process. Although various techniques, including X-ray diffraction (XRD),[2, 3] Fourier transform infrared (FTIR) spectroscopy,[3] total X-ray scattering (TXS),[19] synchrotron-based extended X-ray absorption fine structure spectroscopy (EXAFS),[6, 8, 20-22] and wavelet analysis,[22] have been utilized to characterize the structure of HFA, there is still no agreement on its atomic structure.[8, 19-26] Current views regarding the local atomic structure include the framework model,[8, 25] similar to the structure of scorodite, and the chain model,[20, 21, 23, 24] similar to the structures

60   of butlerite and/or fibroferrite. Both models were proposed mainly based on

61   coordination numbers (CNs) and the interatomic distance of the As-Fe single

62   scattering path derived from shell-fit analysis of As and Fe *K*-edge EXAFS spectra.

63   However, the As-Fe CNs of HFA calculated from EXAFS spectra could vary

64   significantly (1.7 – 4), depending on the fitting strategies and initial model (See

65   Table S1, Supporting Information), thus leading to different conclusions about the

66   local structure of HFA. Chen et al.[8] obtained CNs of 3.2 (As-Fe) and 3.8 (Fe-As) by

67   fitting the EXAFS spectra of HFA and proposed the scorodite-like structure, i.e.,

68   arsenate tetrahedra connecting to four FeO_6 octahedra and vice versa. In comparison,

69   Paktunc and coworkers obtained CNs of approximately 1.8 for both the As-Fe and

70   Fe-As paths, hence suggesting that the local structure of HFA is better described by

71   the chain model, i.e., single chains of corner-sharing FeO_6 octahedra bridged by

72   AsO_4 tetrahedra.[20] Mikutta et al. obtained a Fe-Fe interatomic distance of

73   approximately 5.3 Å according to the wavelet transform analysis and the total X-ray

74   scattering results, which is in agreement with the crystallographic data of scorodite

75   and significantly longer than that of the chain model (approximately 3.8 Å) as in

76   butlerite or fibroferrite.[19, 22] They proposed that HFA was composed of isolated FeO_6

77   octahedra bridged by AsO_4 tetrahedra.

78   Compared to the EXAFS spectra, XANES has much stronger oscillation and is

79   more sensitive to the structural details of the absorbing atoms. Based on full multiple

80   scattering (FMS) calculations, XANES features have been widely adopted to probe

81   the interatomic distance and angle of the local structure during the last two

82   decades.[27-33] Hatada et al. developed the full-potential multiple scattering (FPMS)

83   theory and successfully simulated the XANES spectra of tetrahedrally coordinated

84   cations in $GeCl_4$ or quartz.[34-36] In this study, we used FPMS analysis, in combination

85   with density functional theory (DFT) calculations, EXAFS, and vibrational

86   spectroscopy, to probe the local atomic structure of HFA. This would aid in the

87   understanding of its formation and transformation processes in the environment and

88   hydrometallurgical arsenic removal/fixation operations.

89

90   **EXPERIMENTAL**

91   **Synthesis of Hydrous Ferric Arsenate and Scorodite.** HFA was synthesized

92   using sodium arsenate and ferric sulfate solutions according to a previously reported

93   method.[2, 3] In brief, 0.01 mol of As (from $Na_2HAsO_4 \cdot 7H_2O$) and 0.01 mol of Fe

94   (from $Fe_2(SO_4)_3 \cdot 5H_2O$) were added to 500 mL of double distilled water, and the pH

95   of the mixture was adjusted from 1.3 to 1.8 with a 1 M NaOH solution. Then, the

96   mixture was maintained at that pH and room temperature for 3 hours. The resultant

97   solid product was separated by filtration, washed with HCl solution (pH 1.8), and

98   freeze-dried. Scorodite ($FeAsO_4 \cdot 2H_2O$) was also prepared as a reference material by

99   heating a mixture of 0.3 M Fe(III) and 0.3 M As(V) solutions in an autoclave at

100   175°C for 10 h followed by filtering, rinsing four times with HCl solution (pH 1.8)

101   and freeze drying.[37] Both synthesized materials were characterized using a Rigaku

102   D/Max 2500 X-ray diffractometer with graphite monochromatized $CuK_{\alpha1}$ radiation.

103   The XRD patterns of synthetic HFA showed two broad diffraction peaks at 2θ values

104   of approximately 28° and 58° (Figure S1 in the Supporting Information), which were

105   consistent with previously reported results.[3, 20] After digestion with concentrated

106   hydrochloric acid, the Fe/As molar ratio of HFA was determined to be 1.02±0.01 (n

107   = 3), and the sulfate concentration was lower than 0.01%. The XRD pattern of

108   synthetic scorodite matched well with the standard in the Joint Committee on

109   Powder Diffraction Standards (JSPDS) database (Figure S1).

110   **X-ray Absorption Spectroscopy (XAS) Measurements.** To collect the XAS

111   spectra, approximately 0.1 g of the synthesized solid was pressed as a disc with a

112   diameter of approximately 1 cm after grinding with an agate mortar and pestle. The

113   As and Fe K-edge XAS spectra were obtained on the XAFS beamline at the Beijing

114   Synchrotron Radiation Facility (BSRF). The storage ring was operated at 2.5 GeV

115   and a ring current of 250 mA. A fixed double crystal monochromator with Si(111)

116   crystals was used to monochromatize the white beam. The absolute position of the

117   monochromator was calibrated to 7112 eV for Fe measurements at the first inflection

118   point in the K-edge absorption spectrum of Fe foil and at 11919 eV for As

119   measurements by setting the first inflection point in the L_{III}-edge absorption

120   spectrum of Au foil. The absorption spectra were collected in the energy range of

121   6910-7910 eV for the Fe K-edge spectra and in the range of 11660-12680 eV for the

122   As K-edge spectra in the transmission mode at room temperature. The scan steps

123   were set to 5 eV/step for the pre-edge, 0.5 eV/step for the XANES, and 3-5 eV/step

124   for the EXAFS regions. Each individual sample was scanned three times, and the

125   averaged results are reported.

126   The pre-processing of spectra was performed by using the Athena program in

127   the Demeter package (version, 0.9.20).[38] The pre-edge of all spectra was fitted with a

128   straight line in the range of 150 − 50 eV before the absorption edge. The post-edge

129   absorption background was subtracted by fitting a cubic polynomial spline to the

130   data in the energy range of 0 − 750 eV after the absorption edge. For Fourier

131   transform, the background cutoff parameter (R_{bkg}) was set to 0.9 and 1.0 for As and

132   Fe, respectively.

133   **EXAFS Analysis.** EXAFS data analysis was performed by fitting the Fourier

134   transformed experimental data with the theoretical amplitude and phase functions

135   calculated by FEFF code. The crystallographic structure of scorodite[39] was used as

136   the FEFF input structure for the EXAFS data of scorodite, whereas the structure of

137   HFA optimized by DFT calculations was used as the model structure of HFA. The

138   least-squares fitting was performed in the k ranges of 3–14 Å^{-1} for As and 2–14 Å^{-1}

139   for Fe K-edge spectra with Artemis (Demeter package, version 0.9.20) by using a

140   Kaiser−Bessel window function. Based on the fitting results of scorodite, the

141   amplitude reduction factor, S_0^2, was set to 1.0 and 0.9 for the As and Fe K-edge

142   EXAFS data, respectively.

143   **XANES Analysis.** The X-ray absorption cross sections from the rising edge

144   energy region to 150 eV for As and 200 eV for Fe K-edge XANES spectra after the

145   absorption edge have been analyzed using the recently developed FPMXAN

146   software. For the Fe XANES spectra analysis, the muffin-tin (MT) approximation

147   was used for the shape of the potential.[27, 28, 30] For the As K-edge XANES spectra, a

148   Wigner-Seitz cell was constructed by adding 10 empty spheres around the As atom

149   (Figure S3) based on the FPMS theory.[34-36] The real part of self energy was

150   calculated by using the Hedin-Lunqvist (H-L) potential. Multiple scattering of

151   hydrogen atoms was not considered during the calculations except for the hydrogen

152   atom linked to the central As-O bond. The program used a Monte-Carlo search to

153   alternatively optimize the structure and non-structural parameters (e.g., Fermi energy,

154   energy shift, normalization factor, energy independent broadening, energy dependent

155   broadening, overlapping factor, etc.) until the global minimum of the square residue

156   was achieved. The fitting quality was evaluated using the goodness-of-fit parameter

157   square residue function (S^2), which is defined by the following equation:[27, 28]

158
$$S^2 = n \frac{\sum_{i=1}^{m} w_i \left[\left(y_i^{th} - y_i^{\exp} \right) \varepsilon_i^{-1} \right]^2}{\sum_{i=1}^{m} w_i} \qquad (1)$$

159   where n is the number of independent parameters, m is the number of data points, y_i^{th}

160   and y_i^{exp} are the theoretical and experimental values of the absorption, respectively, ε_i

161   is the error in each point of the experimental data set, and w_i is a statistical weight. In

162   this study, $w_i = 1$ was assumed and the square residual function S^2 was equaled to the

163   statistical χ^2 function.

164   **Molecular Orbital Theory Calculations.** The structure of HFA cluster was

165   optimized by performing DFT calculations using ORCA program (V3.0.3) in the gas

166   phase.[40] All energy minimization calculations were carried out without symmetry

167   and atomic constraints. After preliminary tests, hybrid functional B3LYP and

168   def2-TZVP basis set[41] were utilized for geometric optimization, using the resolution

169   of identity (RI) method. The atom-pairwise dispersion correction with the

170   Becke-Johnson damping scheme (D3BJ)[42] was also applied for all calculations.

171   High-spin Fe^{3+}, with each 3d electron occupying one of the five d-orbitals, was used

172   for energy minimization. The spin multiplicity of the HFA cluster model (containing

173   two Fe atoms) was set to 11 according to multiplicity $= 2S + 1$, where S is the spin of

174   the unpaired electrons.[43] Harmonic vibrational frequencies of the geometrically

175   optimized HFA was also calculated.

176   **Raman Spectroscopy.** The Raman spectra of synthetic HFA and scorodite were

177   collected on a Raman microscope (Thermo Scientific™ DXR™ xi) equipped with a

178   solid state laser diode operating at 785 nm. A 50X objective lens and 0.8 mW laser

179   were applied. Approximately 50 mg of freeze-dried ground sample was mounted on

180   a glass slide. All samples were measured from 60 to 3300 cm^{-1} in the line focus

181   confocal mode with a detector exposure time of 8 s with the accumulation of 30

182   spectra. The wavenumber resolution was set at 4 cm^{-1}. All of the scans were

183   measured at 10% of the laser output at the microscope exit to avoid radiation damage.

184   Before the measurements, the instrument was calibrated to 520 cm^{-1} by using a

185   standard silicon sample.

186   **Infrared Spectroscopy.** FTIR spectra were scanned on a Nicolet 6700 Fourier

187   transform infrared spectrometer (Thermo Fisher Scientific, USA). The spectra were

188   collected in a range of 400–4000 cm^{-1} with a spectral resolution of 4 cm^{-1} and 200

189   co-added scans. Each sample of less than 0.050 mg was mixed with high-purity KBr

190   and then pressed into a disk. Immediately, samples were recorded in the transmission

191   mode. Peak fitting of infrared spectra was performed using a Lorentzian-Gaussian

192   cross function with the minimum number of peaks. All infrared and Raman spectra

193   were manipulated using the software OMNIC (v 8.2).

194

195   **RESULTS AND DISCUSSION**

196   **XANES Analysis.** The normalized As and Fe K-edge XANES spectra of

197   scorodite and HFA are compared in Figure 1a and 1b. The figures show obvious

198   differences at 11876-11888 eV and 11934-11980 eV for As as well as 7126-7135 eV

199   and 7183-7300 eV for Fe K-edge XANES spectra, indicating that the structure of

200   HFA is different from that of scorodite. The As and Fe K-edge XANES spectra of

201   scorodite were simulated using FPMS calculations (Figure 1c and 1d). The

202   crystallographic data of scorodite with the space group $Pcab$ (a = 8.937 Å, b =

203   10.278 Å, c = 9.996 Å, $\alpha = \beta = \gamma = 90°$) were used as the starting simulation model.[39]

204   The cluster radius used is 8 Å, containing 166 and 150 atoms for the As and Fe

205   K-edge XANES spectra simulations, respectively. The results show that the

206   experimental spectra of scorodite were accurately reproduced (S^2 = 7.7 for As and S^2

207   = 3.9 for Fe). The small discrepancy between the theoretical and experimental

208   spectra in the first 20 eV from the edge is possibly due to the limited cluster size or

209   an overestimation of the inelastic losses.[28]

210   The controversy for the local atomic structure of HFA focused on the number

211   and positions of FeO_6 octahedra/AsO_4 tetrahedra coordinating with the central atoms.

212   Since HFA is the precursor of crystalline scorodite,[3, 5] it could be intuitively assumed

213   that FeO_6 octahedra connect with AsO_4 tetrahedra in a similar structure to that of

214   scorodite during the formation of the HFA. Therefore, we extracted the local

215   structure of AsO_4 tetrahedra and FeO_6 octahedra from the crystallographic data of

216   scorodite as the initial structure to distinguish which structure is proximal to the

217   local structure of HFA (Figure 2). The interatomic distances and angles of the

218   extracted local structure are summarized in Table S2 in the Supporting Information.

219   The theoretical As and Fe K-edge XANES spectra of different clusters of AsO_4

220   tetrahedra and FeO_6 octahedra were calculated. Only the non-structural parameters

221   were optimized by fixing the atomic positions of each cluster. The comparisons

222   between the theoretical spectra and experimental data are illustrated in Figure 2c and

223   2d. For As K-edge XANES spectra, it can be observed that the calculated spectrum

224   of the configuration A1, representing one AsO_4 tetrahedron connecting with four

225   FeO_6 octahedra, has significantly stronger oscillations than other clusters in the

226   energy range of 50-80 eV, where it is strongly influenced by the backscattering of Fe

227   atoms. As a result, the S^2 of 6.9 for configuration A1 is higher than those derived

228   from clusters A5, A6, and A7 (one AsO_4 tetrahedron connects with two FeO_6

229   octahedra), indicating that the A1 configuration is not the best. Consistently, the Fe

230   K-edge XANES spectra showed that the configuration F1 (one FeO_6 octahedron

231   connects with four AsO_4 tetrahedra) did not give the smallest S^2 either, implying that

232   the FeO_6 octahedron is less likely to connect with 4 AsO_4 tetrahedra in a manner

233   similar to that of scorodite. These results suggested that in HFA, one AsO_4

234   tetrahedron/FeO_6 octahedron is more likely to connect with two FeO_6

235   octahedra/AsO_4 tetrahedra as a chain rather than a scorodite-like structure.

236   Furthermore, the XANES spectra are also very sensitive to the Fe-O-As angle

237   between AsO_4 tetrahedra and FeO_6 octahedra.[28, 44] It can be clearly observed from

238   Figures 2c and 2d that the clusters of AsO_4 tetrahedra and FeO_6 octahedra with

239   different angles showed different goodness-of-fit parameters, S^2. Simulations for

240   three Fe (As) second-shell neighbors of As (Fe) were also performed (Figure S4,

241   Supporting Information). The clusters A5 ($S^2 = 4.6$) and F5 ($S^2 = 1.0$) showed the

242   best simulation for the experimental data, indicating that the structure of HFA may

243   correspond to a chain structure with AsO_4 tetrahedra connecting to two FeO_6

244   octahedra at vertices through atoms O2 and O3.

245   **Density Functional Theory Calculation Results.** Given that the average

246   crystallite size of the initial HFA precipitates was estimated to be approximately 0.8

247   – 1 nm,[19, 20] the initial structure of HFA cluster with 2 AsO_4 tetrahedra and 2 FeO_6

248   octahedra connecting at vertices through atoms O2 and O3 was constructed based on

249   the XANES simulation results above. Some hydrogen atoms were added to Fe-O

250   bond to achieve charge balance. After energy minimization, the optimized HFA

251   structure showed that the AsO_4 groups occurred as $HAsO_4^{2-}$ group in the middle of

252   the chain and as $H_2AsO_4^-$ at the end of the chain, suggesting a structural formula of

253    $Fe(HAsO_4)_x(H_2AsO_4)_{1-x}(OH)_y \cdot zH_2O$ (hydrous basic ferric hydrogen arsenate,

254    $0.5 < x < 1$, $y = 2-x$) (Figure 3). This result is reasonable because arsenate prefers to exist

255   as protonated arsenate species (i.e., $H_3AsO_4^0$ and $H_2AsO_4^-$) at acidic pH values (pH 1

256   – 2) where HFA precipitates. The calculated bond lengths of As-O in optimized HFA

257   cluster were in the range of 1.62–1.77 Å, with an average of 1.69±0.048 Å. The

258   calculated bond lengths of Fe-O were in the range of 1.85–2.15 Å, with a mean value

259   of 2.01±0.11 Å. The interatomic distance of Fe-Fe was approximately 5.25 Å.

260   Based on the DFT-optimized structure, the As and Fe K-edge XANES spectra

261   of HFA were simulated. It can be observed that the XANES spectra were accurately

262   simulated with $S^2 = 3.3$ for As and $S^2 = 1.3$ for Fe (Figure 4a & 4b), indicating that

263   our chain model is reasonable. Then, the interatomic distances between absorbing

264   atoms and back scattering atoms were optimized for As and Fe K-edge XANES

265   spectra to achieve the best of the As-O and Fe-O bonds. Excellent agreement

266   between the theoretical data and experimental spectra was achieved for both the As

267   ($S^2 = 3.2$) and Fe ($S^2 = 0.19$) K-edge XANES spectra (Figure 4c and 4d). The

268   structural optimization of the XANES spectra gave As-O bond lengths of 1.61 – 1.74

269   Å, with an average of 1.67±0.046 Å, which was comparable to the values derived

270   from DFT calculations and EXAFS data (Table 1). The refined Fe-O bond lengths

271   ranged from 1.84 to 2.15 Å, with an average of 1.99±0.11 Å, which was slightly

272   shorter than those from DFT calculations and EXAFS data (Table 1). In addition, the

273   FPMS optimization of the Fe K-edge XANES spectra gave an average interatomic

274   Fe-Fe distance of 5.22 Å, which is highly consistent with the DFT result (~ 5.25 Å)

275   and the value of approximately 5.3 Å derived from the wavelet analysis reported by

276   Mikutta et al.[7] These results further implied that our chain structure was reasonable

277   for HFA.

278   Paktunc and coworkers argued that the local structure of HFA is similar to those

279   of   the   ferric   sulfates   butlerite   ($FeSO_4(OH) \cdot 2H_2O$)   and   fibroferrite

280   ($FeSO_4(OH) \cdot 5H_2O$), which consist of corner-sharing FeO_6 octahedra single chains

281   bridged by SO_4 tetrahedra.[20, 23, 24] To verify this hypothesis, the structures of butlerite

282   and fibroferrite were modified by replacing the S atoms with As atoms, and were

283   optimized using DFT calculations. The optimized structures are shown in Figure S5

284   in the Supporting Information. The Fe-Fe interatomic distances in optimized

285   butlerite-like and fibroferrite-like structures were 3.78 Å and 3.65 Å on average,

286   respectively, which were significantly shorter than those from the DFT calculations

287   (5.25 Å), the FPMS refinement (5.22 Å) and the wavelet analysis of the Fe K-edge

288   EXAFS data (~5.3 Å).[21] Furthermore, the theoretical As and Fe K-edge XANES

289   spectra calculated using FPMS theory based on the optimized structures were

290   compared with the experimental data. Significant differences were observed for both

291   As ($S^2 = 10.3$ for butlerite and $S^2 = 7.9$ for fibroferrite) and Fe ($S^2 = 2.2$ for butlerite

292   and $S^2 = 4.2$ for fibroferrite) (see Figure S6 in the Supporting Information). These

293   results indicated that the chain structure of corner sharing FeO_6 was unlikely to be a

294   reasonable model to describe the local atomic structure of HFA.

295   **EXAFS Analysis.** Fourier transforms of As and Fe K-edge EXAFS data of

296   synthetic scorodite and HFA are compared in Figure 5. Consistent with previous

297   reports,[8, 22] the magnitudes of the Fourier transform peaks of HFA at R + ΔR ~ 2.9 Å

298   for the As K-edge EXAFS spectra and R + ΔR ~ 3.0 Å for the Fe K-edge EXAFS

299   spectra, with both attributed to the As-Fe oscillations, are less than half of those of

300   crystalline scorodite. This was thought to be the result of lower CNs of the nearest

301 Fe/As atoms around the absorbers or large variation in the Fe-As interatomic

302 distance.[22] The As and Fe K-edge EXAFS spectra were fitted by using the DFT

303 optimized cluster structure of HFA as a model structure. The detailed least-square

304 fitting results are summarized in Table S3 in the Supporting Information. The

305 satisfactory goodness-of-fit parameters, R-factor (0.008 for As and 0.006 for Fe) and

306 reduced χ^2 (110 for As and 28 for Fe), were obtained for both the As and Fe K-edge

307 EXAFS data. As described above, comparisons in Table 1 show that the mean

308 interatomic distances of As-O (1.68 Å, CN = 4), Fe-O (2.00 Å, CN = 6), and As-Fe

309 (3.30 Å, CN = 1.5) are comparable to those derived from DFT calculations and

310 FPMS analysis. These data further demonstrated that the chain structure of HFA

311 proposed in this study is reliable.

312   **Infrared and Raman Spectroscopy.** Figure 6, Figure S7 and Figure S8

313 illustrate the infrared and Raman spectra of synthetic HFA and scorodite. The

314 assignments of infrared and Raman bands for scorodite and HFA are listed in Table

315 S4 in the Supporting Information.

316   The deconvoluted bands of infrared (400 – 1200 cm^{-1}) and Raman spectra (60 –

317 1200 cm^{-1}) for HFA are consistent (Figure 6). Due to the poorly crystalline nature,

318 the bands on infrared and Raman spectra of HFA are poorly resolved and may

319 represent composite of different vibrations. The shape and positions of the infrared

320 and Raman bands of HFA are different from those of scorodite indicating that the

321 protonation and/or metal complexation of AsO_4 tetrahedra in HFA was different from

322 in scorodite.[41, 43, 45] According to the DFT calculated frequencies and previously

323   reported infrared and Raman spectra of (hydrogen) arsenate group-bearing solids

324   (Figure S9 and Table S4),[45-51] the intense HFA infrared bands at 827 and the Raman

325   bands at 825 may be attributed to the composite of v_1 AsO_3 symmetric stretching

326   vibration from $HAsO_4^{2-}$ groups and As-OFe stretching vibrations from $H_2AsO_4^-$

327   groups.[52] The infrared band at 877 cm^{-1} and Raman band at 889 cm^{-1} could be

328   assigned to the v_3 AsO_3 antisymmetric stretching vibration from $HAsO_4^{2-}$ groups.[47-49]

329   The infrared band at 951 cm^{-1} is possibly attributed to the v_3 AsO_2 antisymmetric

330   stretching vibration from $H_2AsO_4^-$ group.[51] The Raman bands at 985 cm^{-1} and weak

331   infrared bands at 1048 and 1108 cm^{-1} may be attributed to the v_1 symmetric

332   stretching vibration of SO_4^{2-} impurity.[50, 53] The shoulder bands at 748 cm^{-1} (infrared)

333   and 766 cm^{-1} (Raman), locating in the range of As-OH stretching vibrations (707–

334   772 cm^{-1})[45-48, 50], could be assigned to the composite of As-OH stretching vibrations

335   from $H_2AsO_4^-$ groups and As-OFe stretching vibrations from $HAsO_4^{2-}$ groups. Other

336   observed bands were assigned to the following vibrations: 213 and 271 cm^{-1} in the

337   Raman spectrum to the lattice vibrations; 424 cm^{-1} of the infrared spectrum and 360

338   and 412 cm^{-1} in the Raman spectrum to the composite of the v_2 $HAsO_4^{2-}$/$H_2AsO_4^-$

339   symmetric bending; 481 cm^{-1} of the infrared spectrum and 469 cm^{-1} of the Raman

340   spectrum to the v_4 $HAsO_4^{2-}$/$H_2AsO_4^-$ antisymmetric bending; and a broad weak band

341   at 605 cm^{-1} in the infrared spectrum to the $FeOH/OH_2$ stretching vibrations and/or

342   As-OH stretching vibrations from $H_2AsO_4^-$ groups.[46-49, 51] Although these results

343   cannot provide clear information on the $HAsO_4^{2-}$/$H_2AsO_4^-$ ratios, the presence of

344   protonated AsO_4 groups in HFA is evidenced by the As-OH stretching vibration

345 bands.

346

347 **IMPLICATIONS**

348   The local atomic structure of synthetic HFA was re-probed using FPMS

349 calculations, EXAFS spectra, DFT calculations, and vibrational spectroscopy. The

350 short chain structure with $HAsO_4^{2-}/H_2AsO_4^-$ tetrahedra and FeO_6 octahedra alternately

351 connected at vertices was found to be a reasonable model for HFA. The butlerite

352 and/or fibroferrite-like chain modes proposed by Paktunc et al.[20] and the

353 scorodite-like model proposed by Chen et al.[8] are unlikely reasonable. The structural

354 information obtained in this study is of significance for understanding the fate of

355 arsenic in some surface environments because HFA is a widely occurring precipitate

356 in the mining-impacted environment and engineered systems, e.g., acid mine drainage

357 and hydrometallurgical tailings,[2, 3, 54] and is the precursor of various crystalline ferric

358 arsenate compounds (i.e., $FeAsO_4 \cdot 2H_2O$, $FeH_3(AsO_4)_2 \cdot 10H_2O$, and

359 $Fe(H_2AsO_4)_3 \cdot 5.5H_2O$) at 25°C depending on the pH values.[5] It would be easier for the

360 HFA with our model structure to convert to ferric hydrogen arsenate minerals

361 $(FeH_3(AsO_4)_2 \cdot 10H_2O$, and $Fe(H_2AsO_4)_3 \cdot 5.5H_2O)$ than the scorodite model which

362 consists of isolated AsO_4 tetrahedron connecting to four FeO_6 octahedra, and vice

363 versa. It is also easier for the structure we proposed to transform to scorodite than the

364 butlerite and/or fibroferrite-like structure consisting of single chains of corner-sharing

365 FeO_6 octahedra bridged by AsO_4 tetrahedra which needs breakage of Fe-O-Fe bonds.

366 The findings of the present work could also explain the reason why HFA showed

367 significantly higher solubility than scorodite[4] which needs to break four covalent

368 bonds to dissolve.

369

370 **ASSOCIATED CONTENT**

371 **Supporting Information.** Additional information contains the XRD patterns, the

372 SEM images, the Wigner-Seitz cell, the DFT-optimized butlerite-like and

373 fibroferrite-like chain structures and their the theoretical As and Fe K-edge XANES

374 spectra, infrared and Raman spectra, previously reported As-Fe CNs, interatomic

375 distance and bond angle in the local scorodite structure, the EXAFS fitting

376 parameters, and frequency assignments.

377

378 **AUTHOR INFROMATION**

379 **Corresponding Author**

380 *Telephone: Tel: +86 (24) 83970503. Email: yongfeng.jia@iae.ac.cn.

381 **Present Address**

382 No.72, Wenhua Road, Shenyang, China, 110016.

383 **Notes**

384 The authors declare no competing financial interest.

385

396

REFERENCES

398   (1) Krause, E.; Ettel, V. A., Solubilities and Stabilities of Ferric Arsenate

399 Compounds. *Hydrometallurgy* **1989,** *22* (3), 311-337.

400   (2) Jia, Y. F.; Xu, L. Y.; Fang, Z.; Demopoulos, G. P., Observation of surface

401 precipitation of arsenate on ferrihydrite. *Environ Sci Technol* **2006,** *40* (10),

402 3248-3253.

403   (3) Jia, Y. F.; Xu, L. Y.; Wang, X.; Demopoulos, G. P., Infrared spectroscopic and

404 X-ray diffraction characterization of the nature of adsorbed arsenate on ferrihydrite.

405 *Geochim Cosmochim Ac* **2007,** *71* (7), 1643-1654.

406   (4) Langmuir, D.; Mahoney, J.; Rowson, J., Solubility products of amorphous

407 ferric arsenate and crystalline scorodite ($FeAsO_4 \cdot 2H_2O$) and their application to

408 arsenic behavior in buried mine tailings. *Geochim Cosmochim Ac* **2006,** *70* (12),

409 2942-2956.

410   (5) Nishimura, T.; Robins, R. G., Crystalline phases in the system

411   Fe(III)-As(V)-H$_2$O at 25C. In *Second International Symposium on Iron control and*

412   *disposal in Hydrometallurgy*, Dutrizac, J.; Harris, G. B., Eds. Canadian Institute of

413   Mining Metallurgy and Petrolenm: Ottawa Canada, 1996; p 521.

414   (6) Maillot, F.; Morin, G.; Juillot, F.; Bruneel, O.; Casiot, C.; Ona-Nguema, G.;

415   Wang, Y. H.; Lebrun, S.; Aubry, E.; Vlaic, G.; Brown, G. E., Structure and reactivity

416   of As(III)- and As(V)-rich schwertmannites and amorphous ferric arsenate sulfate

417   from the Carnoules acid mine drainage, France: Comparison with biotic and abiotic

418   model compounds and implications for As remediation. *Geochim Cosmochim Ac*

419   **2013,** *104*, 310-329.

420   (7) Paktunc, D.; Foster, A.; Heald, S.; Laflamme, G., Speciation and

421   characterization of arsenic in gold ores and cyanidation tailings using X-ray

422   absorption spectroscopy. *Geochim Cosmochim Ac* **2004,** *68* (5), 969-983.

423   (8) Chen, N.; Jiang, D. T.; Cutler, J.; Kotzer, T.; Jia, Y. F.; Demopoulos, G. P.;

424   Rowson, J. W., Structural characterization of poorly-crystalline scorodite,

425   iron(III)-arsenate co-precipitates and uranium mill neutralized raffinate solids using

426   X-ray absorption fine structure spectroscopy. *Geochim Cosmochim Ac* **2009,** *73* (11),

427   3260-3276.

428   (9) Essilfie-Dughan, J.; Hendry, M. J.; Warner, J.; Kotzer, T., Arsenic and iron

429   speciation in uranium mine tailings using X-ray absorption spectroscopy. *Appl*

430   *Geochem* **2012**.

431   (10) Jia, Y. F.; Demopoulos, G. P.; Chen, N.; Cutler, J. N.; Jiang, D. T. In

432   *Preparation, characterization and solubilities of adsorbed and co-precipitated*

433 *iron(III)-arsenate solids*, ***Hydrometallurgy 2003***, PA, Young, C. A.; Alfantazi, A. M.;

434 Anderson, C. G.; Dreisinger, D. B.; Harris, B.; James, A., Eds. TMS: Warrendale: PA,

435 2003; pp 1923-1935.

436 (11) Le Berre, J. F.; Gauvin, R.; Demopoulos, G. P., A study of the crystallization

437 kinetics of scorodite via the transformation of poorly crystalline ferric arsenate in

438 weakly acidic solution. *Colloid Surface A* **2008,** *315* (1-3), 117-129.

439 (12) Dove, P. M.; Rimstidt, J. D., The Solubility and Stability of Scorodite,

440 $FeAsO_4 \cdot 2H_2O$. *Am Mineral* **1985,** *70* (7-8), 838-844.

441 (13) Rochette, E. A.; Li, G. C.; Fendorf, S. E., Stability of arsenate minerals in soil

442 under biotically generated reducing conditions. *Soil Sci Soc Am J* **1998,** *62* (6),

443 1530-1537.

444 (14) Harvey, M. C.; Schreiber, M. E.; Rimstidt, J. D.; Griffith, M. M., Scorodite

445 Dissolution Kinetics: Implications for Arsenic Release. *Environ Sci Technol* **2006,** *40*

446 (21), 6709-6714.

447 (15) Dutrizac, J. E.; Jambor, J. L., The Synthesis of Crystalline Scorodite,

448 Feaso4.2h2o. *Hydrometallurgy* **1988,** *19* (3), 377-384.

449 (16) Filippou, D.; Demopoulos, G. P., Arsenic immobilization by controlled

450 scorodite precipitation. *Jom-Journal of the Minerals Metals & Materials Society*

451 **1997,** *49* (12), 52-55.

452 (17) Demopoulos, G. P.; Droppert, D. J.; Vanweert, G., Precipitation of crystalline

453 scorodite (FeAsO4 · 2H2O) from chloride solutions. *Hydrometallurgy* **1995,** *38* (3),

454 245-261.

455   (18) Singhania, S.; Wang, Q.; Filippou, D.; Demopoulos, G. P., Temperature and

456   seeding effects on the precipitation of scorodite from sulfate solutions under

457   atmospheric-pressure conditions. *Metall Mater Trans B* **2005,** *36* (3), 327-333.

458   (19) Mikutta, C.; Schröder, C.; Marc Michel, F., Total X-ray scattering, EXAFS,

459   and Mössbauer spectroscopy analyses of amorphous ferric arsenate and amorphous

460   ferric phosphate. *Geochim Cosmochim Ac* **2014,** *140*, 708-719.

461   (20) Paktunc, D.; Dutrizac, J.; Gertsman, V., Synthesis and phase transformations

462   involving scorodite, ferric arsenate and arsenical ferrihydrite: Implications for

463   arsenic mobility. *Geochim Cosmochim Ac* **2008,** *72* (11), 2649-2672.

464   (21) Paktunc, D.; Majzlan, J.; Palatinus, L.; Dutrizac, J.; Klementova, M.; Poirier,

465   G., Characterization of ferric arsenate-sulfate compounds: Implications for arsenic

466   control in refractory gold processing residues. *Am Mineral* **2013,** *98* (4), 554-565.

467   (22) Mikutta, C.; Mandaliev, P. N.; Kretzschmar, R., New Clues to the Local

468   Atomic Structure of Short-Range Ordered Ferric Arsenate from Extended X-ray

469   Absorption Fine Structure Spectroscopy. *Environ Sci Technol* **2013,** *47* (7),

470   3122-3131.

471   (23) Paktunc, D., Comment on "Structural characterization of poorly-crystalline

472   scorodite, iron(III)-arsenate co-precipitates and uranium mill neutralized raffinate

473   solids using X-ray absorption fine structure spectroscopy" by N. Chen, DT Jiang, J.

474   Cutler, T. Kotzer, YF Jia, GP Demopoulos and JW Rowson. *Geochim Cosmochim Ac*

475   **2010,** *74* (15), 4589-4596.

476   (24) Paktunc, D.; Manceau, A., Comment on "New Clues to the Local Atomic

477   Structure of Short-Range Ordered Ferric Arsenate from Extended X-ray Absorption

478   Fine Structure Spectroscopy". *Environ Sci Technol* **2013,** *47* (22), 13199-13200.

479   (25) Jiang, D. T.; Chen, N.; Demopoulos, G. P.; Rowson, J. W., Response to the

480   comment on "Structural characterization of poorly-crystalline scorodite,

481   iron(III)-arsenate co-precipitates and uranium mill neutralized raffinate solids using

482   X-ray absorption fine structure spectroscopy". *Geochim Cosmochim Ac* **2010,** *74*

483   (15), 4597-4602.

484   (26) Mikutta, C.; Mandaliev, P. N.; Kretzschmar, R., Response to Comment on

485   "New Clues to the Local Atomic Structure of Short-Range Ordered Ferric Arsenate

486   from Extended X-ray Absorption Fine Structure Spectroscopy". *Environ Sci Technol*

487   **2013,** *47* (22), 13201-13202.

488   (27) Benfatto, M.; Congiu-Castellano, A.; Daniele, A.; Longa, S. D., MXAN: a

489   new software procedure to perform geometrical fitting of experimental XANES

490   spectra. *J Synchrotron Radiat* **2001,** *8*, 267-269.

491   (28) Benfatto, M.; Della Longa, S., Geometrical fitting of experimental XANES

492   spectra by a full multiple-scattering procedure. *J Synchrotron Radiat* **2001,** *8*,

493   1087-1094.

494   (29) Benfatto, M.; Della Longa, S.; Natoli, C. R., The MXAN procedure: a new

495   method for analysing the XANES spectra of metalloproteins to obtain structural

496   quantitative information. *J Synchrotron Radiat* **2003,** *10*, 51-57.

497   (30) Hayakawa, K.; Hatada, K.; Della Longa, S.; D'Angelo, P.; Benfatto, M.,

498   Progresses in the MXAN fitting procedure. *X-Ray Absorption Fine*

499   *Structure-XAFS13* **2007,** *882*, 111-113.

500   (31) Monesi, C.; Meneghini, C.; Bardelli, F.; Benfatto, M.; Mobilio, S.; Manju, U.;

501   Sarma, D. D., Local structure in $LaMnO_3$ and $CaMnO_3$ perovskites: A quantitative

502   structural refinement of Mn K-edge XANES data. *Phys Rev B* **2005,** *72* (17), 174104

503   (pp1-9)

504   (32) Demchenko, I. N.; Denlinger, J. D.; Chernyshova, M.; Yu, K. M.; Speaks, D.

505   T.; Olalde-Velasco, P.; Hemmers, O.; Walukiewicz, W.; Derkachova, A.;

506   Lawniczak-Jablonska, K., Full multiple scattering analysis of XANES at the Cd L-3

507   and O K edges in CdO films combined with a soft-x-ray emission investigation.

508   *Phys Rev B* **2010,** *82* (7), 075107 (pp1-11).

509   (33) Smolentsev, G.; Feiters, M. C.; Soldatov, A. V., Full-potential XANES

510   analysis for 3D local structure investigation of isocyanide Ni complex. *Nucl Instrum*

511   *Meth A* **2007,** *575* (1-2), 168-171.

512   (34) Hatada, K.; Hayakawa, K.; Benfatto, M.; Natoli, C. R., Full-potential

513   multiple scattering for x-ray spectroscopies. *Phys Rev B* **2007,** *76* (6), 060102.

514   (35) Hatada, K.; Hayakawa, K.; Benfatto, M.; Natoli, C. R., Full-potential

515   multiple scattering for core electron spectroscopies. *J Phys-Condens Mat* **2009,** *21*

516   (10), 104206.

517   (36) Hatada, K.; Hayakawa, K.; Benfatto, M.; Natoli, C. R., Full-potential

518   multiple scattering theory with space-filling cells for bound and continuum states. *J*

519   *Phys-Condens Mat* **2010,** *22* (18), 185501.

520   (37) Gomez, M. A.; Assaaoudi, H.; Becze, L.; Cutler, J. N.; Demopoulos, G. P.,

521   Vibrational   spectroscopy   study   of   hydrothermally   produced   scorodite

522   (FeAsO$_4$·2H$_2$O), ferric arsenate sub-hydrate (FAsH; FeAsO$_4$·0.75H$_2$O) and basic

523   ferric arsenate sulfate (BFAS; Fe[(AsO$_4$)$_{(1-x)}$(SO$_4$)$_{(x)}$(OH)$_{(x)}$]·wH$_{(2)}$O). *J Raman*

524   *Spectrosc* **2010,** *41* (2), 212-221.

525   (38) Ravel, B.; Newville, M., ATHENA, ARTEMIS, HEPHAESTUS: data

526   analysis for X-ray absorption spectroscopy using IFEFFIT. *J Synchrotron Radiat*

527   **2005,** *12*, 537-541.

528   (39) Hawthorne, F. C., The hydrogen positions in scorodite. *Acta*

529   *Crystallographica, Section B (Structural Crystallography and Crystal Chemistry)*

530   **1976,** *B32*, 2891-2.

531   (40) Neese, F., The ORCA program system. *Wires Comput Mol Sci* **2012,** *2* (1),

532   73-78.

533   (41) Xu, X. F.; Truhlar, D. G., Accuracy of Effective Core Potentials and Basis

534   Sets for Density Functional Calculations, Including Relativistic Effects, As

535   Illustrated by Calculations on Arsenic Compounds. *J Chem Theory Comput* **2011,** *7*

536   (9), 2766-2779.

537   (42) Grimme, S.; Ehrlich, S.; Goerigk, L., Effect of the Damping Function in

538   Dispersion Corrected Density Functional Theory. *J Comput Chem* **2011,** *32* (7),

539   1456-1465.

540   (43) Watts, H. D.; Tribe, L.; Kubicki, J. D., Arsenic Adsorption onto Minerals:

541   Connecting Experimental Observations with Density Functional Theory Calculations.

542   *Minerals-Basel* **2014,** *4* (2), 208-240.

543   (44) Benfatto, M.; Della Longa, S.; D'Angelo, P., The MXAN procedure: a new

544   method of modeling the XANES spectra to obtain structural quantitative information.

545   *X-Ray and Inner-Shell Processes* **2003,** *652*, 362-369.

546   (45) Myneni, S. C. B.; Traina, S. J.; Waychunas, G. A.; Logan, T. J., Experimental

547   and theoretical vibrational spectroscopic evaluation of arsenate coordination in

548   aqueous solutions, solids, and at mineral-water interfaces. *Geochim Cosmochim Ac*

549   **1998,** *62* (19-20), 3285-3300.

550   (46) Čejka, J.; Sejkora, J.; Bahfenne, S.; Palmer, S. J.; Plášil, J.; Frost, R. L.,

551   Raman spectroscopy of hydrogen-arsenate group (AsO_3OH) in solid-state

552   compounds: cobalt mineral phase burgessite $Co_2(H_2O)_4[AsO_3OH]_2 \cdot H_2O$. *J Raman*

553   *Spectrosc* **2011,** *42* (2), 214-218.

554   (47) Frost, R. L.; Bahfenne, S.; Cejka, J.; Sejkora, J.; Palmer, S. J.; Skoda, R.,

555   Raman   microscopy   of   haidingerite $Ca(AsO_3OH) \cdot H_2O$ and   brassite

556    $Mg(AsO_3OH) \cdot 4H_2O$. *J Raman Spectrosc* **2010,** *41* (6), 690-693.

557   (48) Frost, R. L.; Bahfenne, S.; Čejka, J.; Sejkora, J.; Plášil, J.; Palmer, S. J.,

558   Raman spectroscopic study of the hydrogen-arsenate mineral pharmacolite

559    $Ca(AsO_3OH) \cdot 2H_2O$—implications for aquifer and sediment remediation. *J Raman*

560   *Spectrosc* **2010,** *41* (10), 1348-1352.

561   (49) Sejkora, J.; Čejka, J.; Frost, R. L.; Bahfenne, S.; Plášil, J.; Keeffe, E. C.,

562   Raman spectroscopy of hydrogen-arsenate group (AsO_3OH) in solid-state

563   compounds: copper mineral phase geminite $Cu(AsO_3OH) \cdot H_2O$ from different

564   geological environments. *J Raman Spectrosc* **2010,** *41* (9), 1038-1043.

565   (50) Gomez, M. A.; Becze, L.; Blyth, R. I. R.; Cutler, J. N.; Demopoulos, G. P.,

566   Molecular and structural investigation of yukonite (synthetic & natural) and its

567   relation to arseniosiderite. *Geochim Cosmochim Ac* **2010,** *74* (20), 5835-5851.

568   (51) Chtioui, A.; Benhamada, L.; Jouini, A., Crystal structure, thermal analysis

569   and IR spectroscopic investigation of $(C_6H_9N_2)H_2XO_4$ (X = As, P). *Mater Res Bull*

570   **2005,** *40* (12), 2243-2255.

571   (52) Yang, J. Q.; Chai, L. Y.; Yue, M. Q.; Li, Q. Z., Complexation of arsenate with

572   ferric ion in aqueous solutions. *Rsc Adv* **2015,** *5* (126), 103936-103942.

573   (53) Zhang, D.; Yuan, Z.; Wang, S.; Jia, Y.; Demopoulos, G. P., Incorporation of

574   arsenic into gypsum: Relevant to arsenic removal and immobilization process in

575   hydrometallurgical industry. *J Hazard Mater* **2015,** *300*, 272-280.

576   (54) Murciego, A.; Álvarez-Ayuso, E.; Pellitero, E.; Rodríguez, M. A.;

577   García-Sánchez, A.; Tamayo, A.; Rubio, J.; Rubio, F.; Rubin, J., Study of

578   arsenopyrite weathering products in mine wastes from abandoned tungsten and tin

579   exploitations. *J Hazard Mater* **2011,** *186* (1), 590-601.

580

581 Table 1. Comparison of interatomic distance (Å) (coordination number) of scorodite

582 and HFA among the results derived from crystallographic data (XRD), total X-ray

583 scattering (TXS), As and Fe *K*-edge EXAFS spectra analysis, DFT calculations, and

584 full-potential multiple scattering analysis (FPMS) of As and Fe *K*-edge XANES

585 spectra

	XRD[a]	DFT[b]	XANES[b]	EXAFS[b]	TXS[i]
Scorodite					
As-O	1.67-1.69 (4)	1.68-1.69 (4)	No data	1.69[c] (4)	No data
As-Fe	3.33-3.38 (4)	3.35-3.41 (4)	No data	3.36[c,d] (4)	No data
Fe-O	1.94-2.11 (6)	1.94-2.14 (6)	No data	2.01[d] (6)	No data
Fe-Fe	5.13-5.35 (4)	5.19-5.45 (4)	No data	No data	No data
HFA					
As-O	No data	1.62-1.76 (4)	1.61-1.74 (4) [e]	1.68[c] (4)	1.68
As-Fe	No data	3.21-3.36 (2)	3.16-3.38 (1.5)[f]	3.30[c], 3.33[d] (1.5)	3.32
Fe-O	No data	1.85-2.15 (6)	1.84-2.15 (6) [g]	2.00[d] (6)	1.97
Fe-Fe	No data	5.25 (1)	5.22[g] (1)	5.3[h]	No data

586 [a] The crystallographic data reported by Hawthorne. [b] This study. [c] Data calculated

587 from As *K*-edge EXAFS spectrum. [d] Data calculated from Fe *K*-edge EXAFS

588 spectrum. [e] Data calculated from As *K*-edge XANES spectrum. [f] Averaged value of

589 As-Fe distance from multiple scattering calculation of As and Fe *K*-edge XANES

590 spectrum. [g] Data calculated from Fe *K*-edge XANES spectrum. [h] Data from wavelet

591 analysis of Fe *K*-edge EXAFS data reported by Mikutta et al.[9] [i] Data from total X-ray

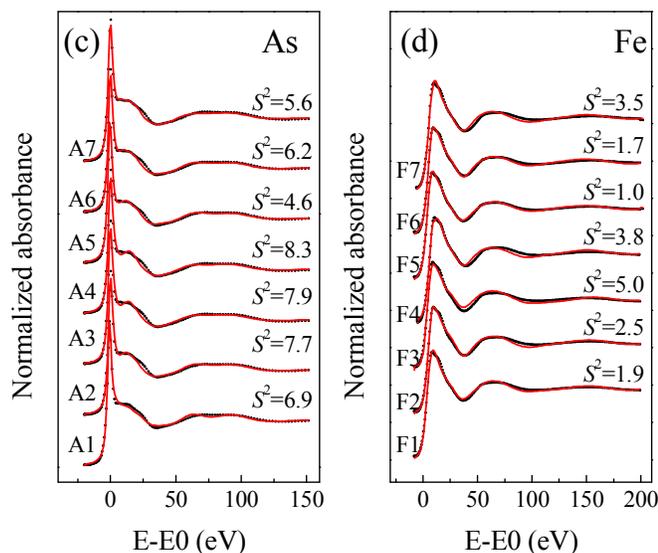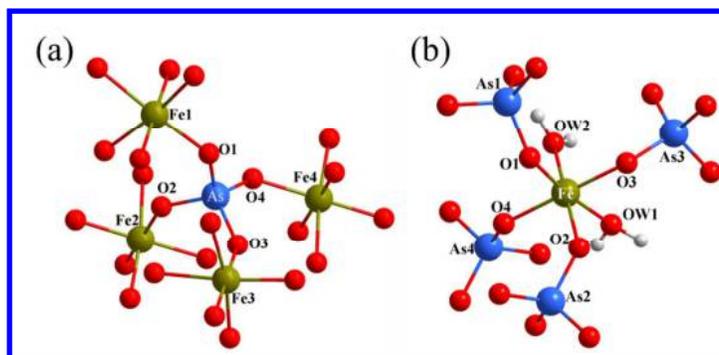592 scattering analysis reported by Mikutta et al.
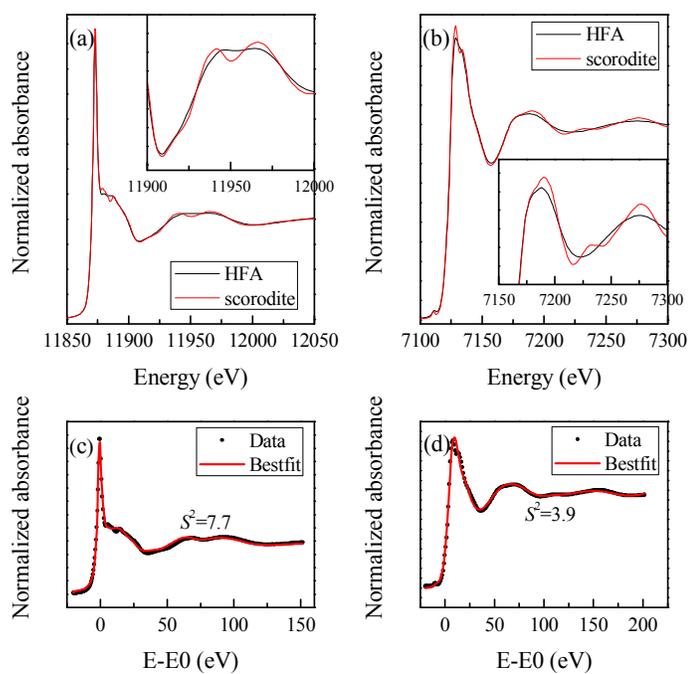
593

594   Figure 1. Arsenic (a) and iron (b) *K*-edge XANES spectra of HFA (black lines) and

595   scorodite (red lines) and the best-fits for As (c) and Fe (d) *K*-edge XANES spectra of

596   scorodite using non-structure optimizations.

597

598

599

Figure 2. Local atomic structure of scorodite. (a) One arsenate tetrahedron coordinates

with four Fe(III)-O octahedra. (b) One Fe(III) octahedron coordinates with four

arsenate tetrahedra. Comparison between theoretical arsenic (c) and iron (d) *K*-edge

XANES spectra (red solid lines) according to the extracted clusters from scorodite

and experimental data (black dotted lines) of HFA. For As *K*-edge spectra, cluster

A1-A7 represent As+4Fe, As+Fe1+Fe2, As+Fe1+Fe3, As+Fe1+Fe4, As+Fe2+Fe3,

As+Fe2+Fe4, and As+Fe3+Fe4, respectively. For Fe *K*-edge spectra, cluster F1-F7

represent Fe+4As, Fe+As1+As2, Fe+As1+As3, Fe+As1+As4, Fe+As2+As3,
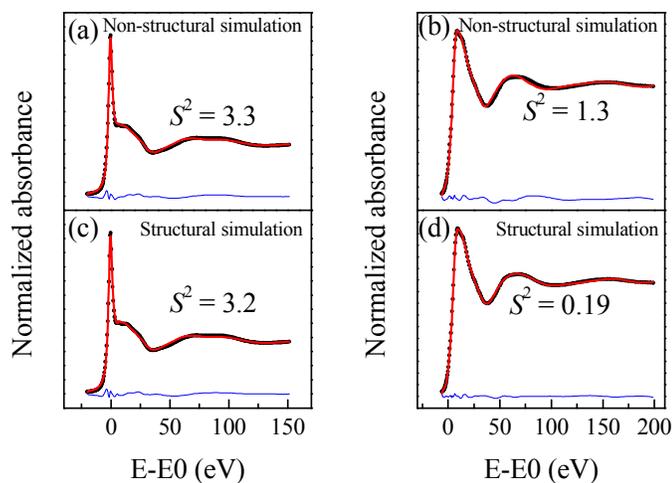
Fe+As2+As4, and Fe+As3+As4, respectively.

31
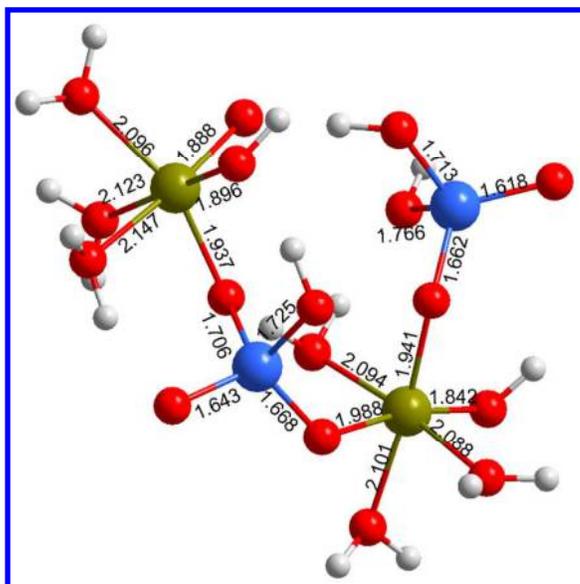
609

610   Figure 3. The DFT optimized structure of hydrous ferric arsenate (HFA) cluster.
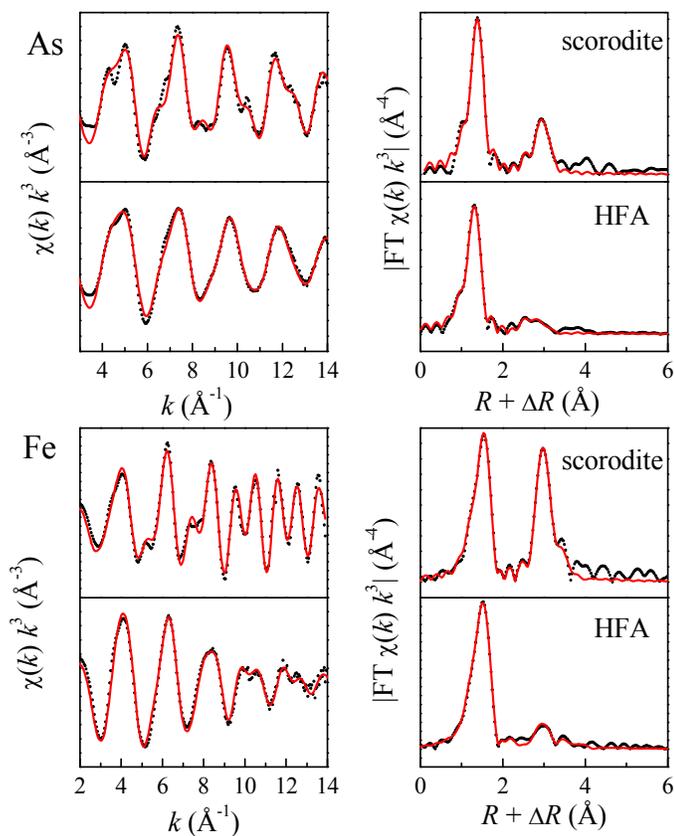
611

32

Figure 4. Comparison of the experimental and theoretical data of non-structural simulation and structural optimized As (left column) and Fe (right column) K-edge XANES spectra of HFA. Experimental data, best fits, and residual are shown as black dots, red lines and blue lines, respectively.
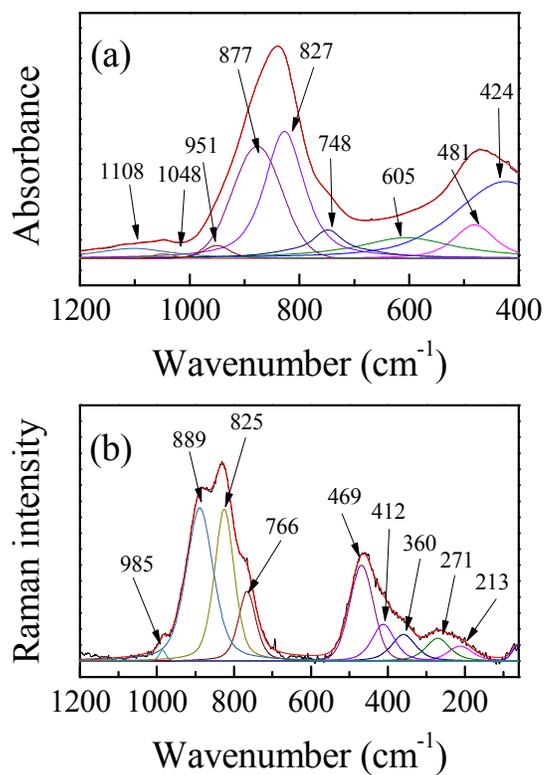
618

Figure 5. Arsenic and iron K-edge k^3-weighted EXAFS spectra (left) and the

corresponding Fourier transforms (right) of scorodite and HFA based on DFT

optimized structure. Experimental data and fits are shown as black dots and red lines,

respectively. The fitting results are summarized in Table S5.

623

34

624

625   Figure 6. Deconvoluted infrared (400 – 1200 cm^{-1}) (b) and Raman (60 – 1200 cm^{-1}) (c)

626   spectra of synthetic scorodite and HFA. Black and red line represent the experimental

627   and fitted spectra, respectively.

628

629   Supporting information to

630   "**New insight into the local structure of hydrous ferric arsenate using**

631   **full-potential multiple scattering analysis, density functional theory calculations,**

632   **and vibrational spectroscopy**"

633

634   Shaofeng Wang[1], Xu Ma[1], Guoqing Zhang[1], Yongfeng Jia[1,2,] *, Keisuke Hatada[3]

635

636   1. Key Laboratory of Pollution Ecology and Environmental Engineering, Institute of

637   Applied Ecology, Chinese Academy of Sciences, Shenyang, 110016, China

638   2. Institute of Environmental Protection, Shenyang University of Chemical

639   Technology, Shenyang, 100049, China

640   3. Département Matériaux Nanosciences, Institut de Physique de Rennes, UMR

641   UR1-CNRS 6251, Université de Rennes 1, 35042 Rennes Cedex, France

642   * Corresponding author, Prof. Yonfeng Jia, Email: yongfeng.jia@iae.ac.cn, Tel: +86

643   24 83970503

644

645   This supporting information contains 9 figures, 4 tables, and references.

36